Electrochemistry Communications 167 (2024) 107799

Contents lists available at ScienceDirect

Electrochemistry Communications

journal homepage: www.elsevier.com/locate/elecom

Long-term electrochemical characterization of novel $Sr_2FeMo_{0.65}Ni_{0.35}O_{6-\delta}$ fuel electrode for high-temperature steam electrolysis in solid oxide cells

Stephanie E. Wolf [a,b], Vaibhav Vibhu [a,*], Pritam K. Chakraborty [a,b], Shibabrata Basak [a], Izaak C. Vinke [a], L.G.J. (Bert) de Haart [a], Rüdiger-A. Eichel [a,b]

[a] Institute of Energy Technologies, Fundamental Electrochemistry (IET-1), Forschungszentrum Jülich GmbH, 52425 Jülich, Germany
[b] Institute of Physical Chemistry, RWTH Aachen University, 52074 Aachen, Germany

ARTICLE INFO

Keywords:
Solid Oxide Electrolysis Cells (SOECs)
Electrochemical performance
Degradation
Post-test analyses
Molybdenum doped strontium ferrite

ABSTRACT

The present study focuses on the highly catalytic double-perovskite $Sr_2FeMo_{0.65}Ni_{0.35}O_{6-\delta}$ (SFMNi) fuel electrode material for Solid Oxide Electrolysis Cells (SOECs). The electrolyte-supported single button cells with the highly active SFMNi fuel electrode were electrochemically characterized between 900 °C down to 750 °C in steam and co-electrolysis conditions using DC- and AC-techniques. The cells achieved current densities of −1.62 A cm^{-2} and −1.74 A cm^{-2} at 900 °C under steam and co-electrolysis conditions, respectively, exceeding the performance of cells with Ni-8YSZ fuel electrodes by ~65–79 % and Ni-GDC fuel electrodes by 24–28 %. The post-test SEM-EDX analyses of the as-prepared and tested cells' cross-section showed increased pore formation and particle growth of the SFMNi fuel electrode after testing in the humidified atmosphere for 500 h.

1. Introduction

High-temperature solid oxide electrolysis cells (SOECs) are an innovative method to produce H_2, which is considered essential for a sustainable transition of the energy system, from renewably generated electricity. However, the long-term system durability remains a key challenge to be solved for a more widespread industrial implementation of SOECs. The SOEC systems have shown several lifetime issues related to the fuel electrode stability in humidified conditions of steam and co-electrolysis. The commonly used Ni cermet electrodes Ni-YSZ and Ni-GDC exhibit rapid aging and subsequent performance loss in high-steam environments due to microstructural changes [1–12]. Therefore, the Mixed-Ionic and Electronic Conducting (MIEC) double perovskite $Sr_2Fe_{2-x}Mo_xO_{6-\delta}$ (SFM) has been considered as an alternative material for increased stability in high-temperature electrolysis. The observed conductivity of SFM in 100 % H_2 at 800 °C of 10–15.3 S·cm^{-1} [13] is, however, two orders of magnitude lower than observed for Ni cermet materials with around 10^3 S·cm^{-1} [14–16]. Therefore, additional B-site doping of SFM with transition metal elements is considered to improve the conductivity as well as the electrocatalytic performance of the electrode material. Previous studies have shown that B-site doped SFM double perovskites exhibit in-situ exsolution of bimetallic alloy nanoparticles under reducing conditions, which improve the conductivity and the catalytic performance of the perovskite material [17,18]. However, long-term durability tests with 500 h have not yet been reported in operating conditions with high steam content to the author's knowledge.

Therefore, we report the surface morphology, electrochemical performance, and long-term durability of B-site doped $Sr_2FeMo_{0.65}Ni_{0.35}O_{6-\delta}$ (SFMNi) for the first time up to 500 h in 50 % steam. The current densities and long-term stability are compared to Ni-8YSZ and Ni-GDC cermet electrodes. The evolution of cell voltage under constant current load is linked to the microstructural post-test analysis of the cells' cross-section.

2. Experimental

2.1. Powder preparation

The SFMNi powder was synthesized via the solid-state synthesis route with the precursors $SrCO_3$ (Aldrich chem, 99 %), Fe_2O_3 (Alfa Aesar, 99 %), MoO_3 (Alfa Aesar, 99 %), and NiO (Alfa Aesar, 99 %). The precursor powders were weighed in, ball milled for 4 h at 250 rpm using zirconia balls and isopropanol (VWR, 99.8 %), and subsequently dried overnight. After annealing at 1250 °C for 8 h in air, the obtained powders were crushed and milled again to obtain a mean particle size of

* Corresponding author.
E-mail address: v.vibhu@fz-juelich.de (V. Vibhu).

https://doi.org/10.1016/j.elecom.2024.107799
Received 6 June 2024; Received in revised form 26 August 2024; Accepted 29 August 2024
Available online 31 August 2024

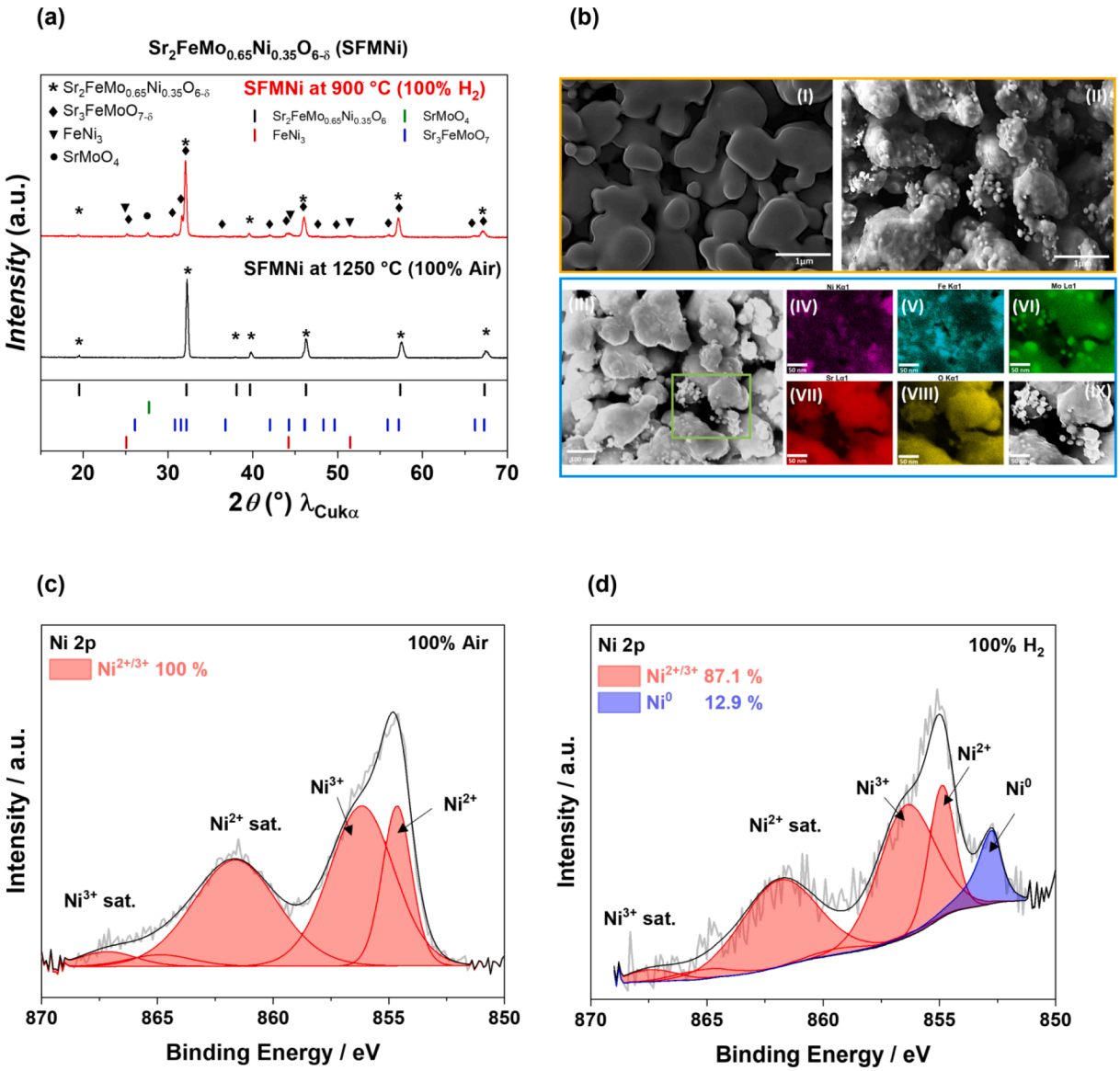

Fig. 1. (a) XRD pattern of the as-prepared SFMNi powder sintered in air at 1250 °C, and after reduction in 100 % H_2 for 8 h at 900 °C. (b) SEM image of (I) as-prepared and, (II) reduced SFMNi electrode, (III) High magnification SEM-EDX image of the reduced SFMNi electrode illustrating the contrast features in green boxes, and (IV-VIII) elemental mapping of the corresponding particles in (IX). XPS scans of SFMNi powder sintered in (c) air and (d) after reduction for 8 h in 100 % H_2.

about 1 μm. The $La_{0.58}Sr_{0.4}Co_{0.2}Fe_{0.8}O_{3-\delta}$ (LSCF) oxygen electrode powder was prepared using previously dried La_2O_3 (Aldrich, 99 %) with a modified Pechini method [19].

2.2. Cell preparation

The electrolyte-supported single cells (ESCs) were prepared using 8YSZ electrolyte supports (Kerafol®, ∅ = 2 cm and thickness ≈ 250 μm). The $Ce_{0.8}Gd_{0.2}O_{1.9}$ (GDC) interlayer (∅ = 1.8 cm) was first deposited on both sides by screen printing and sintered at 1375 °C for 1 h. The fuel electrode, i.e., SFMNi (∅ = 1.2 cm) was then deposited on one side of electrolyte support and sintered at 1150 °C for 2 h. The LSCF oxygen electrode layer was screen printed on the other side and sintered at 1080 °C for 3 h. A thin Au layer (∅ = 1.2 cm) was printed as a current-collecting layer on the SFMNi fuel electrode prior to the electrochemical measurements. The active area of the single cell was 0.79 cm^2.

2.3. Electrochemical characterization

The single button cells were mounted in the full ceramic measurement housing and sealed with a gold gasket [13]. Au and Pt current collectors were used to connect the fuel and the oxygen electrode, respectively. The single cells were heated to 900 °C in N_2 gas flow at the fuel electrode and air on the oxygen electrode side. The SFMNi fuel electrode was reduced by gradually increasing H_2 from 0 % to 100 % balanced with N_2 [20]. The current–voltage characteristics (I-V curves) of single cells were measured using a Vertex.5A Potentiostat/Galvanostat system (Ivium Technologies®, Eindhoven, Netherlands) with varied potential from 0.6 V up to 1.5 V under various gas compositions. The long-term durability tests were carried out in 50 % H_2O + 50 % H_2 at 900 °C under constant current load of -0.5 A·cm^{-2}.

2.4. Scanning electron microscopy (SEM)

Using a Scanning Electron Microscope (Quanta FEG 650, FEI

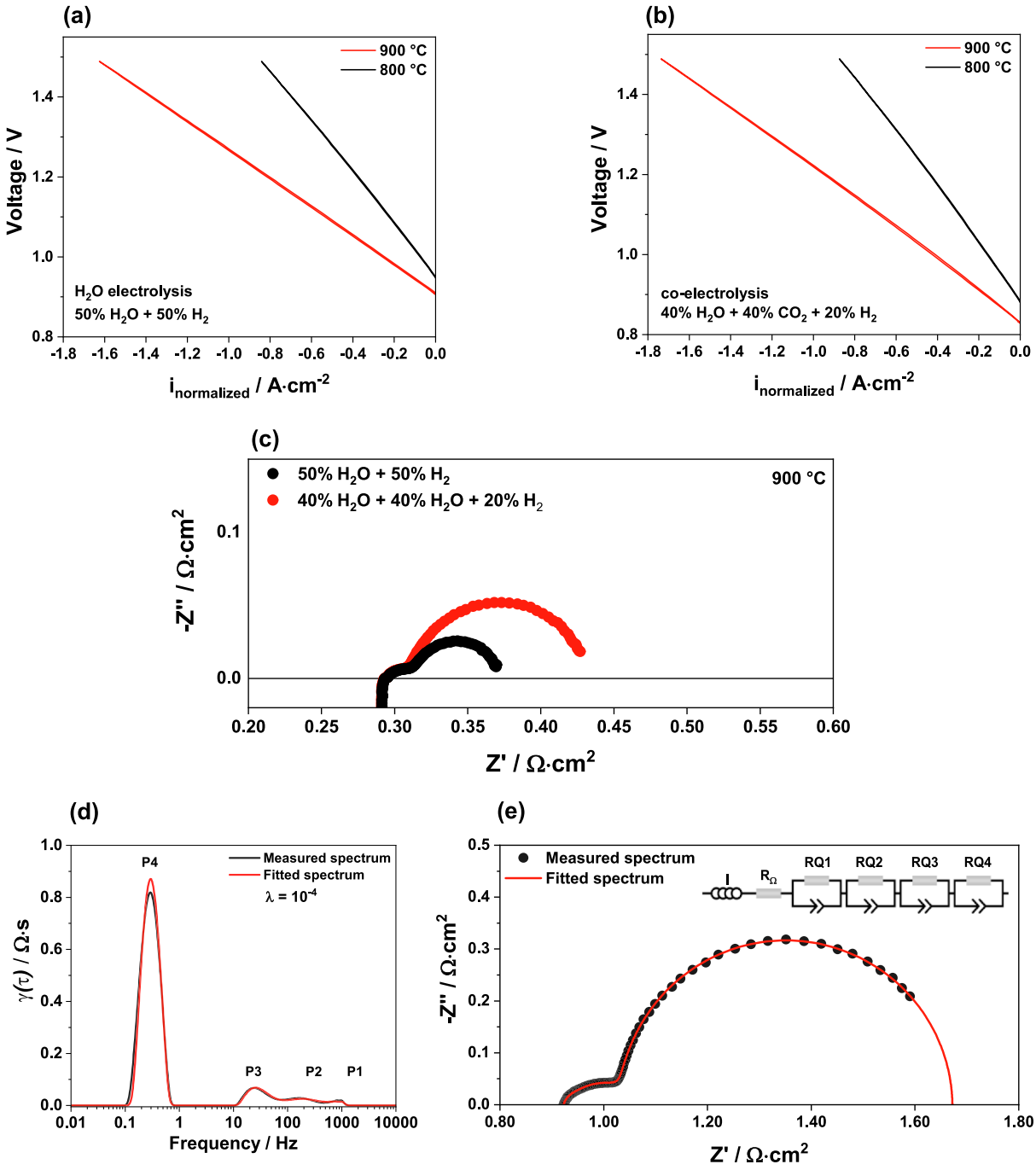

Fig. 2. IV curves measured at 900 °C and 800 °C for SFMNi single cell in (a) steam electrolysis, (b) co-electrolysis conditions, (c) Impedance spectra measured in steam electrolysis and co-electrolysis conditions at 900 °C and OCV, (d) DRT of the experimental and fitted impedance data for SFMNi at 750 °C in steam electrolysis recorded at OCV, and (e) Nyquist plot of the experimental and fitted data with the used Equivalent Circuit model (ECM).

equipped with an Energy-Dispersive X-Ray Spectroscopy (EDX) detector, USA), the as-prepared and tested single button cells and powders were characterized by at 10–20 kV. The powders were characterized by the Tescan AmberX (Tecan Group, Czech Republic) field emission-SEM-EDX with 20 kV.

2.5. X-ray photoelectron spectroscopy (XPS)

The samples were reduced at 900 °C in 100 % H_2 for 72 h. For the XPS analysis, a Phi5000 VersaProbeII (ULVAC-Phi Inc., USA) instrument was used. The spectra were recorded at 15 keV and − 50 W with an X-ray beam size of 200 μm using monochromatic Al Kα irradiation.

The high-resolution analyses were carried out between 10 eV and 30 eV in steps of 0.1 eV step and an analyzer pass energy of 23.5 eV. For data analysis, the results were charge-corrected to the 1 s carbon spectrum at 285.0 eV and a nonlinear Shirley-type background was employed.

3. Results and discussion

3.1. Material characterization

The room temperature X-Ray Diffraction (XRD) patterns of the as-prepared and reduced powdered $Sr_2FeMo_{0.65}Ni_{0.35}O_{6-\delta}$ (SFMNi)

Table 1
Electrochemical performance of the $Sr_2FeMo_{0.65}Ni_{0.35}O_{6-\delta}$ fuel electrode in comparison to state-of-the-art Ni-cermet electrodes with varied atmospheres at 900 °C.

Fuel Electrode	Test conditions @ 900 °C	$R_{P\ @OCV}$/ Ω·cm^2	$i_{@1.5V}$/ A·cm^{-2}	Ref.
Ni-8YSZ	50 % H_2O + 50 % H_2	0.17	–0.91	[34]
	40 % H_2O + 40 % CO_2 + 20 % H_2	0.20	–1.06	[34]
Ni-GDC	50 % H_2O + 50 % H_2	0.06	–1.31	[34]
	40 % H_2O + 40 % CO_2 + 20 % H_2	0.09	–1.37	[34]
$Sr_2FeMo_{0.65}Ni_{0.35}O_{6-\delta}$	50 % H_2O + 50 % H_2	0.10	–1.62	This work
	40 % H_2O + 40 % CO_2 + 20 % H_2	0.14	–1.74	

[a]All cells were prepared in the configuration FE/GDC/8YSZ/GDC/LSCF with the same precursor materials, pastes, and supported on a 250 m thick 8YSZ electrolyte.
GDC: $Ce_{0.8}Gd_{0.2}O_{1.9}$, 8YSZ: 8 mol% YSZ, LSCF: $La_{0.58}Sr_{0.4}Co_{0.2}Fe_{0.8}O_{3-\delta}$.

samples are shown in Fig. 1a. After sintering the powder at 1250 °C in air for 8 h, the pattern reveals the formation of phase double perovskite SFMNi, as indicated by the peaks at 19.5° and 39.6° (ICSD 168704) [21]. After the reduction of the powdered SFMNi at 900 °C for 8 h in 100 % H_2, the XRD pattern exhibits several new peaks. The peaks at ~44.25° and ~51.37° suggest the exsolution of $FeNi_3$ alloy nanoparticles (ICSD 103557) from the perovskite matrix, thereby forming also $Sr_3FeMoO_{7-\delta}$ observed at 42° (ICSD 156787) [22]. A small fraction of $SrMoO_4$ was detected at 27.7° (ICSD 99089) [23]. The exsolved $FeNi_3$ nanoparticles were visualized in high-resolution SEM-EDX images seen in Fig. 1b. The secondary electron SEM images of the SFMNi samples before (I) and after reduction in 100 % H_2 (II) respectively show a change from a smooth and homogenous to a rough surface due to exsolved spherical sub-micron nanoparticles observed on the surface (III). The EDS mapping in IV-VIII shows the presence of Fe-, Ni- and Mo-rich exsolutions measuring 10–50 nm. The elemental distribution of all other elements is relatively even throughout the particle. The XPS scans of SFMNi in air and after reduction in 100 % H_2 for 8 h at 900 °C are depicted in Fig. 1c-d.

The fitted spectra exhibit double peak features representing the Ni (2p) core levels for SFMNi. The oxidized sample in Fig. 1c shows multiple peaks with binding energies of 854.8 eV and 856.3 eV representing the core levels of Ni^{2+} ($2p_{3/2}$) and Ni^{3+} ($2p_{3/2}$), respectively. The peak around 861.7 eV has been classified as satellite of Ni^{2+} ($2p_{3/2}$) [24]. The satellite peak of Ni^{3+} ($2p_{3/2}$) has been observed in previous studies at 866.1 eV by Dubey et al. [24], while Biesinger et al. [25,26] and Grosvenor et al. [27] have fitted two peaks in this range at 864.7 eV and 867.0 eV for Ni $2p_{3/2}$. In Fig. 1c, two peaks can be seen at 864.9 eV and 867.2 eV as well. When changing the measurement conditions from air (Fig. 1c) to H_2 (Fig. 1d), the oxidation state of the sample is partially reduced from 100 % Ni^{2+}/Ni^{3+} to ~87 % Ni^{2+}/Ni^{3+} and ~13 % Ni^0 (852.7 eV) [28]. These results support the XRD patterns and SEM images that show a partial phase change from SFMNi in hydrogen atmosphere and exsolved $FeNi_3$ nanoparticles. The exsolved nanoparticles exhibit higher conductivities, and improved catalytic activity compared to the bulk phase, which leads to enhanced electrochemical material performance [17,22,29,30]. In the case of B-site doped double perovskite structures like SFMNi, the formation of catalytically active bimetallic Fe-Ni alloy nanoparticles has been observed under reducing conditions and at elevated temperatures [31–33].

3.2. Electrochemical impedance characterization

The electrochemical performance of single button cells with an SFMNi fuel electrode was characterized with current–voltage characteristics and electrochemical impedance spectroscopy for steam (50 % H_2O + 50 % H_2) and co-electrolysis (40 % H_2O + 40 % CO_2 + 20 % H_2) as depicted in Fig. 2 and listed in Table 1. Current densities of –1.62 A·cm^{-2} and –1.74 A·cm^{-2} were obtained in steam and co-electrolysis respectively at 1.5 V and 900 °C. In comparison to Ni-8YSZ and Ni-GDC, the SFMNi fuel electrode exhibits an improved performance by 79 % and 24 % in steam and 65 % and 28 % in co-electrolysis at 1.5 V. Previous comparison of the fuel electrode material $Sr_2Fe_{1.3}Ni_{0.2}Mo_{0.5}O_{6-\delta}$ mixed with $Sm_{0.2}Ce_{0.8}O_{1.9}$ (SDC) compared to $Sr_2Fe_{1.5}Mo_{0.5}O_{6-\delta}$-SDC in humified conditions showed an increased current density from –0.64 A·cm^{-2} at 850 °C and 1.3 V for SFM-SDC to –1.26 A·cm^{-2} with the addition of Ni [17]. The higher current density was attributed to the higher relative surface due to exsolved Fe-Ni nanoparticles.

3.2.1. Equivalent circuit model evaluation

Impedance spectra were taken under different measurement conditions, such as variations of temperature and gas composition. To evaluate the experimental data, the number of time constants was analyzed by the Distribution of Relaxation Times (DRT) method with a regularization parameter λ of 10^{-4} resulting in an Equivalent Circuit Model Evaluation (ECM) with an inductor, a serial resistor followed by four RQ elements connected in series. In Fig. 2d, the DRT spectrum for SFMNi measured at 750 °C in steam electrolysis at OCV is depicted as an example and shows four peaks P1, P2, P3, and P4. The experimental impedance data and the fit shown in Fig. 2e agree qualitatively well. The low X^2 error of 10^{-7} between the fitted and experimental data indicates a reasonable ECM as well.

3.3. Temperature variation

The performance of single cells with an SFMNi fuel electrode was characterized in steam electrolysis and co-electrolysis conditions between 750 °C and 900 °C in steps of 25 °C to determine the underlying thermally activated processes. In the Nyquist plots, two distinct arcs can be discerned with one at lower and the other one at higher frequencies (Fig. 2, Fig. 3). Throughout all temperature ranges, the dominance of the low-frequency arc compared to its high-frequency counterpart is evident. Both arcs exhibit an increase in magnitude as the operational temperature decreases, indicating thermally activated processes. The ASR increases consequently from 0.37 Ω·cm^2 to 1.29 Ω·cm^2 in steam electrolysis and from 0.43 Ω·cm^2 to 1.23 Ω·cm^2 in co-electrolysis conditions when decreasing the operation temperature from 900 °C to 750 °C. In addition, the temperature variation has a discernible impact on the ohmic resistance R_Ω and polarization resistance R_P. The activation energy for R_Ω is determined based on the slope of the Arrhenius equation and equals between 56 ± 2 kJ·mol^{-1}. This closely aligns with values reported in the literature for the ionic conductivity in YSZ electrolyte films and suggests that the primary contribution to R_Ω is the thick 8YSZ electrolyte [35–37]. The impact of the thermally activated process independent of the experimental gas composition, can also be observed in the DRT spectra and the corresponding Nyquist plots in Fig. 3a-d. For steam and co-electrolysis, the DRT spectra exhibit four distinct time constants P1, P2, P3, and P4 that increase in magnitude with decreasing operating temperature. The process associated with P4 (1.1–0.33 Hz) dominates the DRT spectra over the whole temperature range under steam as well as co-electrolysis conditions in comparison to P1, P2, and P3. This makes P4 the major contributing process to the cell resistance irrespective of operating conditions, called the rate-limiting process. The peaks P1 (2655–1115 Hz), P2 (200–100 Hz), and P3 (25–12 Hz) increase less pronounced with temperature and shift to slightly higher frequencies in the case of P1 and P2 as well as to slightly lower frequencies for P3. In the subsequent discussion of individual process resistances, the circuit elements R_{RQ1}, R_{RQ2}, R_{RQ3}, and R_{RQ4} correspond to the peaks P1, P2, P3, and P4. The detailed Arrhenius analysis is shown in Fig. 3e-f.

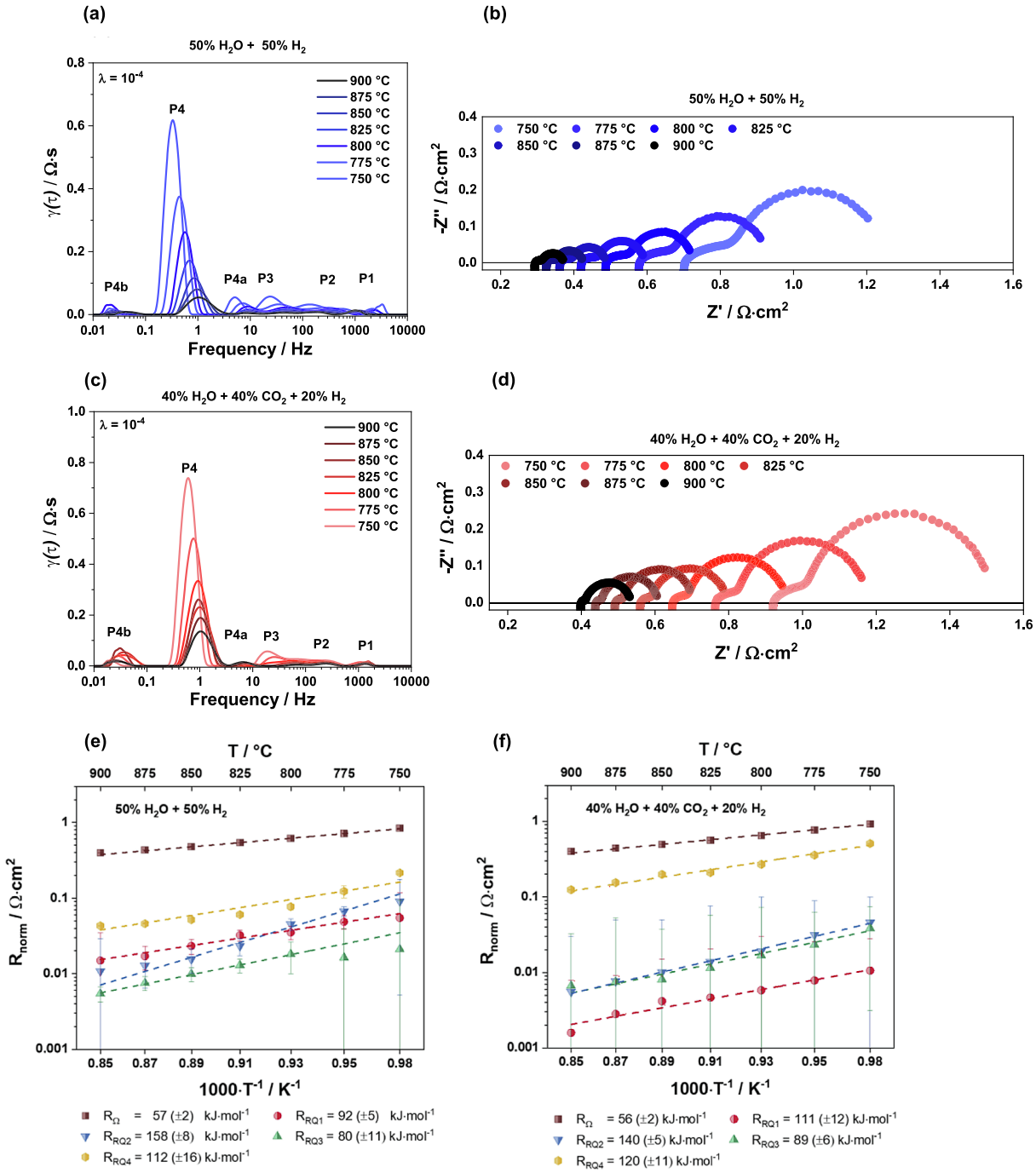

Fig. 3. DRT spectra and corresponding Nyquist plots measured at OCV from 900 °C to 750 °C in (a, b) steam electrolysis, and (c, d) co-electrolysis for SFMNi single cell. The temperature-dependent process resistance analysis in (e) steam electrolysis, and (f) co-electrolysis for SFMNi single cell.

The activation energy of the rate-limiting process P4 was observed to be 112 ± 16 kJ·mol^{-1} and 120 ± 11 kJ·mol^{-1} for steam and co-electrolysis, respectively. Previous studies have suggested that within this frequency range, the observed processes include the conversion of gases and diffusion phenomena taking place at the fuel electrode side [35,38,39]. However, these processes exhibit minimal thermal activation, making it inappropriate to attribute them to P4 [40–42]. The process P4 shows a distinct impact by polarization variation. This suggests a Butler-Volmer type behavior and indicates that P4 is related to the charge transfer process at the fuel electrode side, observed in MIECs within the frequency range of 1–2 Hz, accompanied by an activation energy of approximately107-126 kJ·mol^{-1} [36]. In the mid to low-frequency range, R_{RQ3} (P3, 25–12 Hz) unveils a distinctive activation energy closely tied to the selection of the gas stream at the fuel and oxygen electrode side. For $Sr_2FeMo_{0.65}Ni_{0.35}O_{6-\delta}$, the determined activation energy is 80–89 ± 11 kJ·mol^{-1}. Previous studies suggested an overlap of fuel and oxygen electrode mechanisms, e.g., transport processes [38]. The high-frequency contribution P1 modeled by R_{RQ1} (2655–1115 Hz) shows activation energies of 92 ± 5 kJ·mol^{-1} in steam and 111 ± 12 kJ·mol^{-1} in co-electrolysis for SFMNi. The middle to high-frequency process modeled by R_{RQ2} (200–100 Hz) shows activation energies between 140 – 158 ± 8 kJ·mol^{-1} for both steam and co-electrolysis. The thermally influenced processes in this frequency range have been attributed to the surface exchange kinetics and oxygen diffusion in the bulk and at the surface of the LSCF electrode as well as to an electrode charge-transfer process at the LSCF oxygen electrode

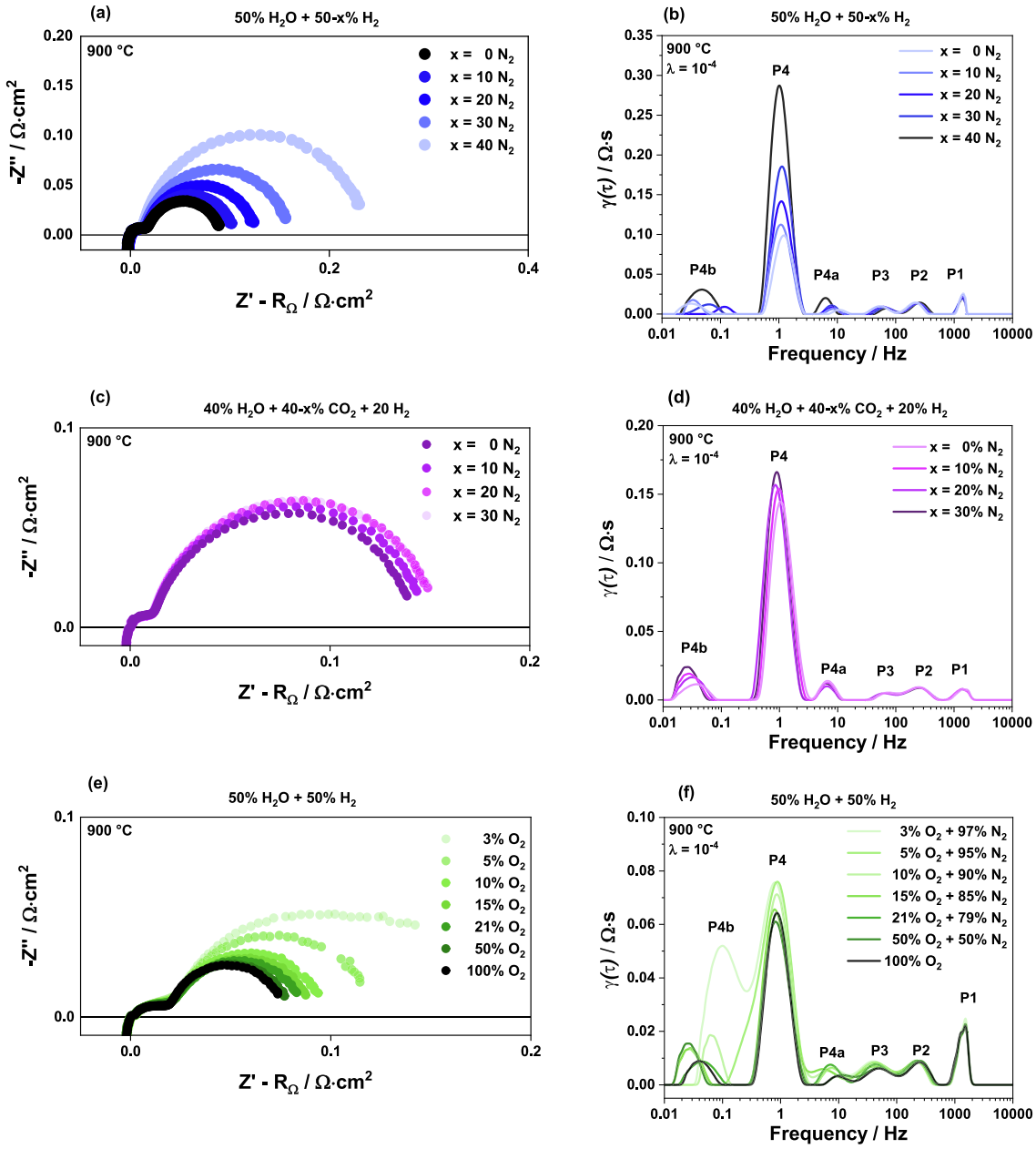

Fig. 4. (a) Nyquist plot and (b) the corresponding DRT spectra for the fuel gas variation of H_2O-H_2. (c) Nyquist plot and (d) DRT spectra for the variation of H_2O-CO_2-H_2. (e) Nyquist plots and (f) corresponding DRT spectra for the variation of O_2-N_2 content at the oxygen electrode side in steam electrolysis conditions.

[36,38,41,43,44].

3.4. Gas variation at the fuel and oxygen electrode

The in-depth process analysis was further corroborated by the variation of gas composition at the fuel and oxygen electrode side to identify the distinct impedance contributions from the two electrodes. The recorded impedance spectra as well as the corresponding DRT spectra are shown in Fig. 4a-f. In steam electrolysis, the steam content was kept constant, while the H_2 content was systematically reduced from 50 % to 10 % balanced with N_2. The corresponding Nyquist plot and DRT spectra for the fuel gas variation are illustrated in Fig. 4a-b. With reduced H_2 content at the fuel electrode, the total area specific resistance (ASR) increases from 88 mΩ·cm^2 with 50 % H_2O + 50 % H_2 to 230 mΩ·cm^2 measured in an atmosphere of 50 % H_2O + 10 % H_2 + 40 % N_2. In co-electrolysis, the CO_2 was varied from 40 % to 10 %, which led to an increased ASR from 146 mΩ·cm^2 to 159 mΩ·cm^2 (Fig. 4c-d). The results emphasize that the gas variation is mainly influencing the low-frequency process P4, which is increasing with decreasing H_2 gas at the fuel electrode. The processes P1, P2, and P3 are less impacted by the gas variation.

To explore the role of the oxygen electrode in the impedance spectra, the oxygen partial pressure was systematically varied from 0.03 to 1 atm balanced with N_2 at the oxygen electrode balanced with a constant fuel gas composition of 50 % H_2O + 50 % H_2. The Nyquist plots and the corresponding DRT spectra in Fig. 4e and Fig. 4f illustrate negligible changes for P1, P2, and P3, while P4 increases slightly with decreasing pO_2. Data from previous studies of symmetrical LSCF cells measured in varied N_2-O_2 mixtures identified P1 and P2 as physical processes at the oxygen electrode side [36]. The impact of pO_2 in the mid-frequency range between 100–10 Hz and the low-frequency process around 1 Hz decreases with increasing pO_2, wherefore an overlap of different fuel

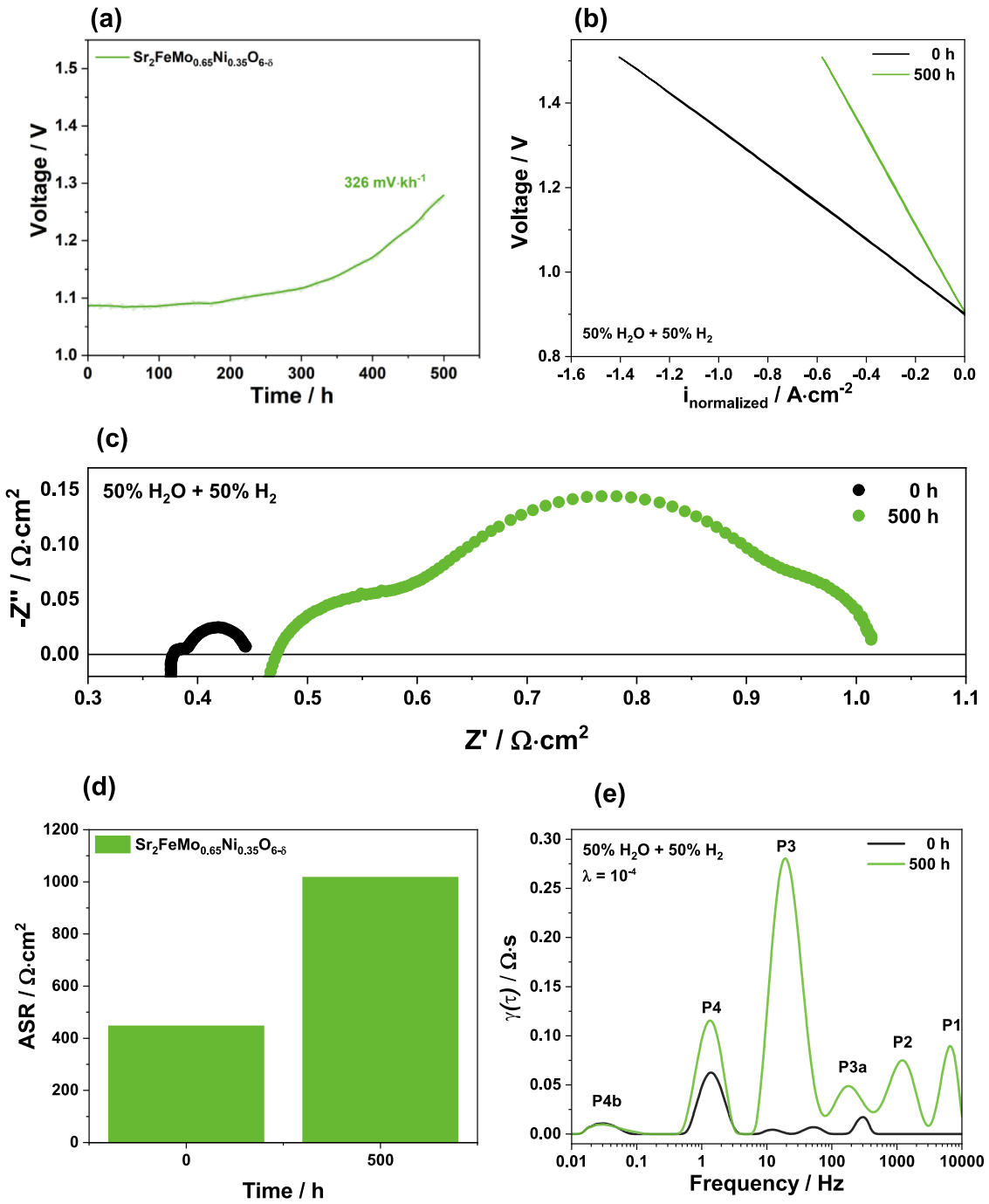

Fig. 5. (a) Long-term stability test of single cells with a cell composition of SFMNi/GDC/8YSZ/GDC/LSCF in steam electrolysis under constant current load of –0.5 A·cm^{-2} at 900 °C for 500 h. Comparison of (a) the current–voltage characteristics, (b) the Nyquist plots (c) the ASR, and (d) the corresponding DRT spectra recorded before and after the long-term measurement.

and oxygen electrode processes was theorized. P1, P2, and P3 observed in single cells with an LSCF oxygen electrode were assigned to the charge transfer process in the oxygen electrode (P1) and oxygen surface exchange kinetics as well as oxygen bulk diffusion (P2, P3) [35,36].

3.5. Long-term stability

3.5.1. Electrochemical analysis

The SFMNi fuel electrode was tested at 900 °C for 500 h under a constant current density of –0.5 A·cm^{-2}. The measured cell voltage curve is shown in Fig. 5a and depicts a stable linear trend for the first 100 h in the fuel gas atmosphere of 50 % H_2O + 50 % H_2. Thereafter, the cell voltage increases continuously up to 193 mV (326 mV·kh^{-1}). The electrolyte-supported single cell with a state-of-the-art Ni-YSZ fuel electrode exhibits a much higher degradation rate than SFMNi with 760 mV·kh^{-1} within the first 100 h [34]. The single cell with a Ni-GDC fuel electrode has shown a degradation rate of 499 mV·kh^{-1} in 50 % H_2O + 50 % H_2 at 900 °C at –0.5 A·cm^{-2} [35]. Current-voltage characteristics and impedance spectra were recorded before and after the degradation test to analyze the degradation impact on the individual process resistances. The results are given in Fig. 5b and Fig. 5c, respectively. The maximum current density decreases from –1.41 A·cm^{-2} to –0.58 A·cm^{-2}, i.e. by 59 %, after the durability test at 900 °C for 500 h in steam electrolysis. The Nyquist plots before and after the degradation

Table 2
Resistance evolution of SFMNi fuel electrode as a function of operation time in steam electrolysis during 500 h durability testing at 900 °C under a constant load of −0.5 A·cm^{-2}.

Time/h	Resistances/mΩ·cm^2						
	R_Ω	R_{RQ1}	R_{RQ2}	R_{RQ3}	R_{RQ4}	R_P	ASR
SFMNi							
0	375	5	6	5	54	70	445
500	442	185	74	224	93	576	1017

test in Fig. 5c show a notable increase in both ohmic and polarization resistances.

The single button cell with the high-performing SFMNi fuel electrode exhibits a total ASR increase of 572 mΩ·cm^2 after 500 h (Fig. 5d). The fitted impedance results are listed in Table 2 and illustrate the contribution of R_Ω and R_P to the ASR increase over time. R_Ω accounts for around 12 % and R_P contributes the main share of 88 % to the ASR increase. As seen from Table 2 and the DRT analysis in Fig. 5e, all individual resistances increase over time. The process resistance R_{RQ3} contributes mainly to the R_P increase with 219 mΩ·cm^2, followed by R_{RQ1} (180 mΩ·cm^2). The process resistances R_{RQ2}, and R_{RQ4} show only a small increase of 68 mΩ·cm^2 and 39 mΩ·cm^2 respectively. The DRT analysis depicts as well, a frequency shift of R_{RQ1}, $R_{RQ2,}$ and R_{RQ3} to higher frequencies.

3.5.2. *Microstructural post-test analysis*

As shown previously in Fig. 1, the exsolved $FeNi_3$ particles are partially embedded in the parent oxide surface and have been shown to be more resilient to particle agglomeration compared to the deposited analogs, thus improving the electrode stability at high temperatures [45]. The microstructure of as-prepared and tested SFMNi fuel electrodes was characterized with SEM-EDX to determine structural changes. The samples were encased in epoxy resin, polished, and sputtered with gold before undergoing analysis. Fig. 6 illustrates the cross-sections of as-prepared and SFMNi fuel electrodes after operation in electrolysis mode. The electrolyte remained unchanged, and no electrode delamination was observed. Notably, the electrode microstructure shows increased pore formation and particle growth after the long-term test in humidified conditions. This result corresponds to the observed degradation rate and increase in ASR shown in Table 2 and Fig. 5. The cross-sectional SEM-EDX analysis of the as-prepared and operated LSCF oxygen electrodes is displayed in Fig. 6b. Similar to the previous results for the LSCF oxygen electrode, a slight Sr segregation through the pores of the GDC barrier layer and subsequent formation of an insulating $SrZrO_3$ layer is observed, which may have led to the increase in ohmic resistance throughout the degradation test [36].

3.5.3. *Conclusion*

In this study, the electrocatalytic active SFMNi was evaluated as fuel electrode material for SOECs. The high-resolution SEM imaging and the XPS spectra confirmed phase conversion and Fe-Ni nanoparticle exsolution in operating conditions. The performance and long-term stability of electrolyte-supported single cells with SFMNi were characterized in humidified conditions. Current densities of –1.62 A·cm^{-2} were achieved for steam electrolysis and –1.74 A·cm^{-2} in co-electrolysis conditions at 1.5 V and 900 °C. The results show higher performance than cells with state-of-the-art Ni-8YSZ as well as with Ni-GDC fuel electrodes. The durability test under a constant current load of −0.5 A·cm^{-2} was performed in steam electrolysis conditions at 900 °C for 500 h. The measured cell voltage curve showed a degradation rate of 326 mV·kh^{-1}, which was found to be lower than for Ni-8YSZ and Ni-GDC. Current-voltage characteristics and impedance spectra recorded before and after the degradation test underlined that the cell performance decreased after the test by around 59 %. The SEM-EDX post-test analysis revealed increased pore formation and particle growth of the SFMNi electrode after the long-term test in steam electrolysis. In addition, slight Sr segregation through the pores of the GDC barrier layer led to $SrZrO_3$ layer formation and increased ohmic resistance.

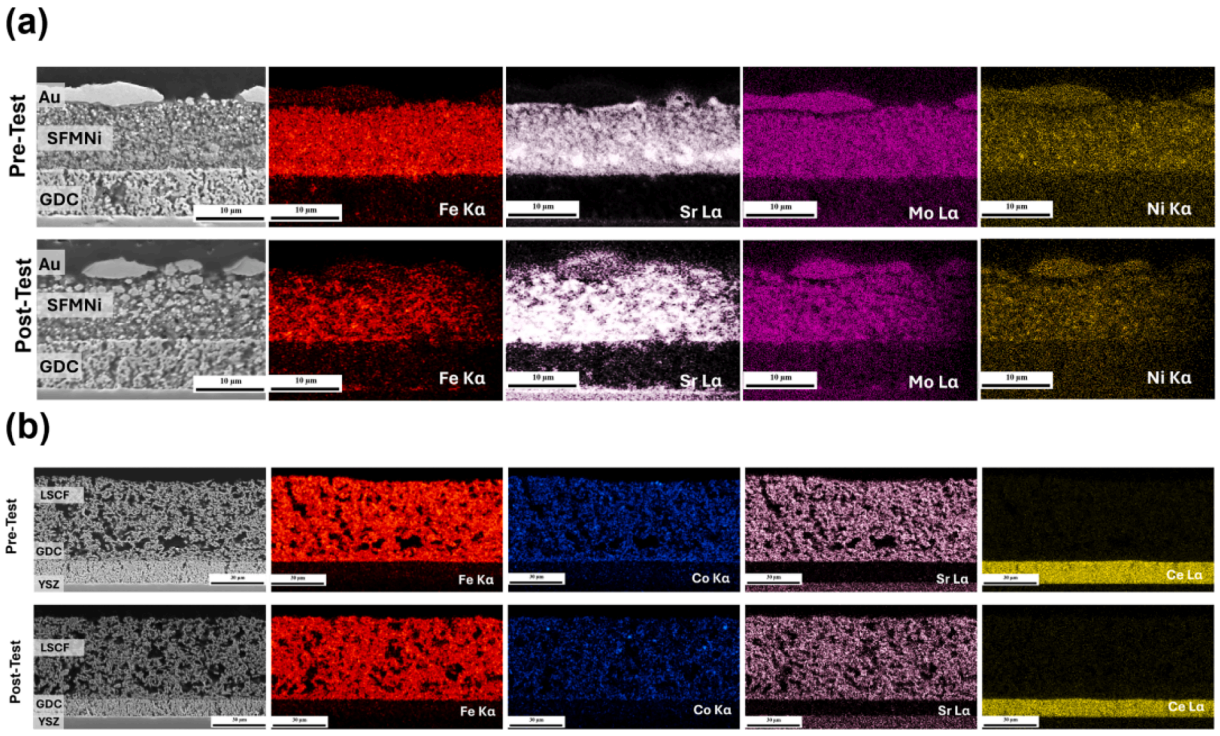

Fig. 6. (a) Cross-sectional SEM-EDX mapping of the fuel electrode side for Sr (Lα, 13.89 keV), Fe (Kα, 6.40 keV), Mo (Lα, 17.14 keV), Ni (Kα, 7.47 keV) lines before and after the long-term test of 500 h in steam electrolysis at –0.5 A·cm^{-2} and 900 °C. (b) Cross-sectional SEM-EDX mapping of the oxygen electrode side for Fe (Kα, 6.40 keV), Ce (Lα, 33.90 keV), Co (Kα, 6.93 keV), Sr (Lα, 13.89 keV) lines before and after the long-term test.

CRediT authorship contribution statement

Stephanie E. Wolf: Writing – review & editing, Writing – original draft, Visualization, Validation, Methodology, Investigation, Formal analysis, Conceptualization. **Vaibhav Vibhu:** Writing – review & editing, Visualization, Validation, Supervision, Methodology, Conceptualization. **Pritam K. Chakraborty:** Investigation. **Shibabrata Basak:** Visualization, Validation, Supervision. **Izaak C. Vinke:** Visualization, Validation, Supervision, Resources. **L.G.J. (Bert) de Haart:** Supervision, Software, Resources, Project administration, Funding acquisition. **Rüdiger-A. Eichel:** Supervision, Software, Resources, Project administration, Funding acquisition.

Declaration of competing interest

The authors declare that they have no known competing financial interests or personal relationships that could have appeared to influence the work reported in this paper.

Data availability

Data will be made available on request.

Acknowledgments

The author gratefully acknowledges funding by the German Federal Ministry of Education and Research (BMBF) within the SOC-Degradation 2.0 project: Transfer of knowledge into products for a “Green Hydrogen” vector - Impedance analysis of intrinsic and extrinsic degradation mechanisms in SOC cells and repeat units (FKZ 03SF0621A). We acknowledge the support of Hitachi High-Technologies. The authors gratefully acknowledge Dr. Heinrich Hartmann from the Institute Central Institute for Engineering, Electronics and Analytics (ZEA-3) for the performance of XPS measurements.

References

[1] M. Trini, A. Hauch, S. de Angelis, X. Tong, P.V. Hendriksen, M. Chen, J. Power Sources 450 (2020) 227599, https://doi.org/10.1016/j.jpowsour.2019.227599.
[2] F. Tietz, D. Sebold, A. Brisse, J. Schefold, J. Power Sources 223 (2013) 129–135, https://doi.org/10.1016/j.jpowsour.2012.09.061.
[3] M. Hubert, J. Laurencin, P. Cloetens, B. Morel, D. Montinaro, F. Lefebvre-Joud, J. Power Sources 397 (2018) 240–251, https://doi.org/10.1016/j.jpowsour.2018.06.097.
[4] P.S. Jørgensen, J.R. Bowen, ECS Trans. 35 (2011) 1655–1660, https://doi.org/10.1149/1.3570152.
[5] D. The, S. Grieshammer, M. Schroeder, M. Martin, M. Al Daroukh, F. Tietz, J. Schefold, A. Brisse, J. Power Sources 275 (2015) 901–911, https://doi.org/10.1016/j.jpowsour.2014.10.188.
[6] G. Rinaldi, S. Diethelm, E. Oveisi, P. Burdet, J. van Herle, D. Montinaro, Q. Fu, A. Brisse, Fuel Cells 17 (2017) 541–549, https://doi.org/10.1002/fuce.201600194.
[7] Q. Fang, C.E. Frey, N.H. Menzler, L. Blum, J. Electrochem. Soc. 165 (2018) F38–F45, https://doi.org/10.1149/2.0541802jes.
[8] M.P. Hoerlein, M. Riegraf, R. Costa, G. Schiller, K.A. Friedrich, Electrochim. Acta 276 (2018) 162–175, https://doi.org/10.1016/j.electacta.2018.04.170.
[9] M. Trini, P.S. Jørgensen, A. Hauch, J.J. Bentzen, P.V. Hendriksen, M. Chen, J. Electrochem. Soc. 166 (2019) F158–F167, https://doi.org/10.1149/2.1281902jes.
[10] E. Lay-Grindler, J. Laurencin, J. Villanova, P. Cloetens, P. Bleuet, A. Mansuy, J. Mougin, G. Delette, J. Power Sources 269 (2014) 927–936, https://doi.org/10.1016/j.jpowsour.2014.07.066.
[11] M. Keane, H. Fan, M. Han, P. Singh, Int. J. Hydrogen Energy 39 (2014) 18718–18726, https://doi.org/10.1016/j.ijhydene.2014.09.057.
[12] M.B. Mogensen, A. Hauch, X. Sun, M. Chen, Y. Tao, S.D. Ebbesen, K.V. Hansen, P. V. Hendriksen, Fuel Cells 17 (2017) 434–441, https://doi.org/10.1002/fuce.201600222.
[13] S.E. Wolf, V. Vibhu, C.L. Coll, N. Eyckeler, I.C. Vinke, R.-A. Eichel, L.G.J. de Haart, ECS Trans. 111 (2023) 2119–2130, https://doi.org/10.1149/11106.2119ecst.
[14] S.E. Wolf, F.E. Winterhalder, V. Vibhu, L.G.J. de Haart, O. Guillon, R.-A. Eichel, N. H. Menzler, J. Mater. Chem. A 11 (2023) 17977–18028, https://doi.org/10.1039/D3TA02161K.
[15] M.H. Pihlatie, A. Kaiser, M. Mogensen, M. Chen, Solid State Ion. 189 (2011) 82–90, https://doi.org/10.1016/j.ssi.2011.02.001.
[16] S. Aruna, M. Muthuraman, K. Patil, Solid State Ion. 111 (1998) 45–51, https://doi.org/10.1016/S0167-2738(98)00187-8.
[17] Y. Wang, T. Liu, M. Li, C. Xia, B. Zhou, F. Chen, J. Mater. Chem. A 4 (2016) 14163–14169, https://doi.org/10.1039/C6TA06078A.
[18] G. Xiao, S. Wang, Y. Lin, Z. Yang, M. Han, F. Chen, J. Electrochem. Soc. 161 (2014) F305–F310, https://doi.org/10.1149/2.061403jes.
[19] V. Vibhu, I.C. Vinke, F. Zaravelis, S.G. Neophytides, D.K. Niakolas, R.-A. Eichel, L. G.J. de Haart, Energies 15 (2022) 2726, https://doi.org/10.3390/en15082726.
[20] S.E. Wolf, V. Vibhu, E. Tröster, I.C. Vinke, R.-A. Eichel, L.G.J. de Haart, Energies 15 (2022) 5449, https://doi.org/10.3390/en15155449.
[21] Y. Yang, Z. Yang, Y. Chen, F. Chen, S. Peng, J. Electrochem. Soc. 166 (2019) F109–F113, https://doi.org/10.1149/2.0701902jes.
[22] Z. Du, H. Zhao, S. Yi, Q. Xia, Y. Gong, Y. Zhang, X. Cheng, Y. Li, L. Gu, K. Świerczek, ACS Nano 10 (2016) 8660–8669, https://doi.org/10.1021/acsnano.6b03979.
[23] A. Felli, L. Duranti, M. Marelli, M. Dosa, E. Di Bartolomeo, M. Piumetti, M. Boaro, J. Electrochem. Soc. 170 (2023) 114511, https://doi.org/10.1149/1945-7111/ad06e7.
[24] P. Dubey, N. Kaurav, R.S. Devan, G.S. Okram, Y.K. Kuo, RSC Adv. 8 (2018) 5882–5890, https://doi.org/10.1039/c8ra00157j.
[25] Mark C. Biesinger, Brad P. Payne, Leo W. M. Lau, Andrea Gerson, Roger St. C. Smart, Surf. Interface Anal. 41 (2009) 324–332. doi: 10.1002/sia.3026.
[26] M.C. Biesinger, B.P. Payne, A.P. Grosvenor, L.W. Lau, A.R. Gerson, R.S. Smart, Appl. Surf. Sci. 257 (2011) 2717–2730, https://doi.org/10.1016/j.apsusc.2010.10.051.
[27] A.P. Grosvenor, M.C. Biesinger, R.S. Smart, N.S. McIntyre, Surf. Sci. 600 (2006) 1771–1779, https://doi.org/10.1016/j.susc.2006.01.041.
[28] C.J. Powell, X-ray Photoelectron Spectroscopy Database XPS,Version 4.1, NIST Standard Reference Database 20, National Institute of Standards and Technology, 1989.
[29] C. Zhao, Y. Li, W. Zhang, Y. Zheng, X. Lou, B. Yu, J. Chen, Y. Chen, M. Liu, J. Wang, Energy Environ. Sci. 13 (2020) 53–85, https://doi.org/10.1039/c9ee02230a.
[30] M.L. Weber, M. Wilhelm, L. Jin, U. Breuer, R. Dittmann, R. Waser, O. Guillon, C. Lenser, F. Gunkel, ACS Nano 15 (2021) 4546–4560, https://doi.org/10.1021/acsnano.0c08657.
[31] J. Mei, T. Liao, Z. Sun, Mater. Today Energy 31 (2023) 101216, https://doi.org/10.1016/j.mtener.2022.101216.
[32] X. Xi, X.-W. Wang, Y. Fan, Q. Wang, Y. Lu, J. Li, L. Shao, J.-L. Luo, X.-Z. Fu, J. Power Sources 482 (2021) 228981, https://doi.org/10.1016/j.jpowsour.2020.228981.
[33] A.J. Carrillo, J.M. Serra, Catalysts 11 (2021) 741, https://doi.org/10.3390/catal11060741.
[34] I.D. Unachukwu, V. Vibhu, J. Uecker, I.C. Vinke, R.-A. Eichel, L.G.J. de Haart, ECS Trans. 111 (2023) 1445–1452, https://doi.org/10.1149/11106.1445ecst.
[35] I.D. Unachukwu, V. Vibhu, I.C. Vinke, R.-A. Eichel, L.G.J. de Haart, J. Power Sources 556 (2023) 232436, https://doi.org/10.1016/j.jpowsour.2022.232436.
[36] J. Uecker, I.D. Unachukwu, V. Vibhu, I.C. Vinke, R.-A. Eichel, L.G.J. de Haart, Electrochim. Acta 452 (2023) 142320, https://doi.org/10.1016/j.electacta.2023.142320.
[37] F. Kundracik, M. Hartmanová, J. Müllerová, M. Jergel, I. Kostič, R. Tucoulou, Mater. Sci. Eng. B 84 (2001) 167–175, https://doi.org/10.1016/S0921-5107(01)00515-3.
[38] P. Caliandro, A. Nakajo, S. Diethelm, J. van Herle, J. Power Sources 436 (2019) 226838, https://doi.org/10.1016/j.jpowsour.2019.226838.
[39] A. Weber, J. Szász, S. Dierickx, C. Endler-Schuck, E. Ivers-Tiffée, ECS Trans. 68 (2015) 1953–1960, https://doi.org/10.1149/06801.1953ecst.
[40] S.D. Ebbesen, M. Mogensen, J. Power Sources 193 (2009) 349–358, https://doi.org/10.1016/j.jpowsour.2009.02.093.
[41] S. Primdahl, Solid State Ion. 152–153 (2002) 597–608, https://doi.org/10.1016/S0167-2738(02)00393-4.
[42] V. Sonn, A. Leonide, E. Ivers-Tiffée, J. Electrochem. Soc. 155 (2008) B675, https://doi.org/10.1149/1.2908860.
[43] D. Papurello, D. Menichini, A. Lanzini, Electrochim. Acta 258 (2017) 98–109, https://doi.org/10.1016/j.electacta.2017.10.052.
[44] D.G. Goodwin, H. Zhu, A.M. Colclasure, R.J. Kee, J. Electrochem. Soc. 156 (2009) B1004, https://doi.org/10.1149/1.3148331.
[45] C. Li, Y. Deng, L. Yang, B. Liu, D. Yan, L. Fan, J. Li, L. Jia, Adv. Powder Mater. 2 (2023) 100133, https://doi.org/10.1016/j.apmate.2023.100133.